

Bottom-up structural proteomics: cryoEM of protein complexes enriched from the cellular milieu

Chi-Min Ho^{1,2,3,10}, Xiaorun Li^{3,4,10}, Mason Lai^{2,3}, Thomas C. Terwilliger⁵, Josh R. Beck^{6,7}, James Wohlschlegel⁸, Daniel E. Goldberg⁶, Anthony W. P. Fitzpatrick⁹ and Z. Hong Zhou^{1,2,3*}

X-ray crystallography often requires non-native constructs involving mutations or truncations, and is challenged by membrane proteins and large multicomponent complexes. We present here a bottom-up endogenous structural proteomics approach whereby near-atomic-resolution cryo electron microscopy (cryoEM) maps are reconstructed ab initio from unidentified protein complexes enriched directly from the endogenous cellular milieu, followed by identification and atomic modeling of the proteins. The proteins in each complex are identified using cryoID, a program we developed to identify proteins in ab initio cryoEM maps. As a proof of principle, we applied this approach to the malaria-causing parasite *Plasmodium falciparum*, an organism that has resisted conventional structural-biology approaches, to obtain atomic models of multiple protein complexes implicated in intraerythrocytic survival of the parasite. Our approach is broadly applicable for determining structures of undiscovered protein complexes enriched directly from endogenous sources.

The recent ‘resolution revolution’ in cryoEM^{1–9} has opened the door for determination of high-resolution structure of a vast number of previously intractable biological systems. There is no need for crystallization because samples for cryoEM are preserved in a frozen-hydrated state and are randomly oriented within a layer of vitreous ice. Without the need to introduce mutations or truncations that provide better crystal contacts, it is possible to observe proteins in native or near-native biologically relevant states with cryoEM. Moreover, with a dramatically reduced requirement for both quantity and homogeneity of samples for cryoEM, we are no longer restricted to systems that can be produced in large quantities at high purity. In fact, cryoEM has the added advantage of the potential for achieving multiple high-resolution structures of several different conformational states of a single protein complex¹⁰, or even several structures of completely unrelated protein complexes in the same sample, from a single cryoEM dataset.

By leveraging the latest cutting-edge innovations in cryoEM, it is now possible to accommodate the low yields and heterogeneity of samples enriched directly from endogenous sources. However, this approach introduces an intriguing challenge: if we obtain a near-atomic-resolution (3.0–4.0 Å) cryoEM map of a protein complex from a heterogeneous sample, how do we identify the protein(s) this map represents?

In instances where an unidentified protein is crystallized, the high purity (low complexity) of the sample and the high resolutions (1.5–2.5 Å) of crystallographic density maps make identification of the unknown protein trivial^{11–14}. However, identifying protein(s) in cryoEM maps from heterogeneous mixtures enriched directly from endogenous sources is extremely challenging owing to the large pool of potential candidates and the varying local resolutions and low overall resolutions (compared with crystallography) of 3.0–4.0 Å that are typical

of routinely achievable cryoEM maps. A systematic approach for identifying a complex from typical near-atomic (3.0–4.0 Å) cryoEM maps would be transformative for cryoEM and systems biology, opening the door for structure determination of novel, unidentified molecules and complexes enriched directly from endogenous sources.

To address this challenge, we have developed a targeted bottom-up endogenous structural proteomics approach whereby protein complexes are enriched directly from the cellular milieu and identified by imaging and structure determination using mass spectrometry and near-atomic resolution cryoEM density maps reconstructed ab initio (Fig. 1). This workflow employs our program, cryoID, to semiautonomously identify proteins in cryoEM maps at better than 4.0 Å resolution without any prior knowledge of the sequence(s). As a proof of principle, we have applied this approach to *P. falciparum*, an organism that has proven recalcitrant to typical structural-biology approaches¹⁵. By directly imaging components of the parasite cell lysate, we obtained multiple near-atomic-resolution structures of protein complexes implicated in the pathogenesis of malarial parasites, from a single cryoEM dataset. We then used cryoID to unambiguously assign side chains and identify the complex, enabling atomic model building.

Results

Workflow. Our workflow consists of the following five steps, starting from raw cell lysates and potentially yielding atomic models of many native macromolecular complexes:

Step 1: Endogenous purification. We use sucrose gradient fractionation to enrich protein complexes from raw cell lysates of endogenous sources (Fig. 1a).

Step 2: Sample evaluation. We then assess the complexity of each fraction by SDS–polyacrylamide gel electrophoresis (SDS–PAGE) and negative-stain EM (Fig. 1b,c and Supplementary Fig. 1).

¹The Molecular Biology Institute, University of California, Los Angeles, CA, USA. ²Department of Microbiology, Immunology, & Molecular Genetics, University of California, Los Angeles, CA, USA. ³California NanoSystems Institute, University of California, Los Angeles, CA, USA. ⁴Hefei National Laboratory for Physical Sciences at the Microscale, School of Life Sciences, University of Science and Technology of China, Hefei, Anhui, China.

⁵Los Alamos National Laboratory and the New Mexico Consortium, Los Alamos, NM, USA. ⁶Departments of Medicine and Molecular Microbiology, Washington University School of Medicine in St. Louis, St. Louis, MO, USA. ⁷Department of Biomedical Sciences, Iowa State University, Ames, IA, USA.

⁸Department of Biological Chemistry, David Geffen School of Medicine, University of California, Los Angeles, CA, USA. ⁹Zuckerman Institute, Columbia Medical School, New York, NY, USA. ¹⁰These authors contributed equally: Chi-Min Ho, Xiaorun Li. *e-mail: Hong.Zhou@UCLA.edu

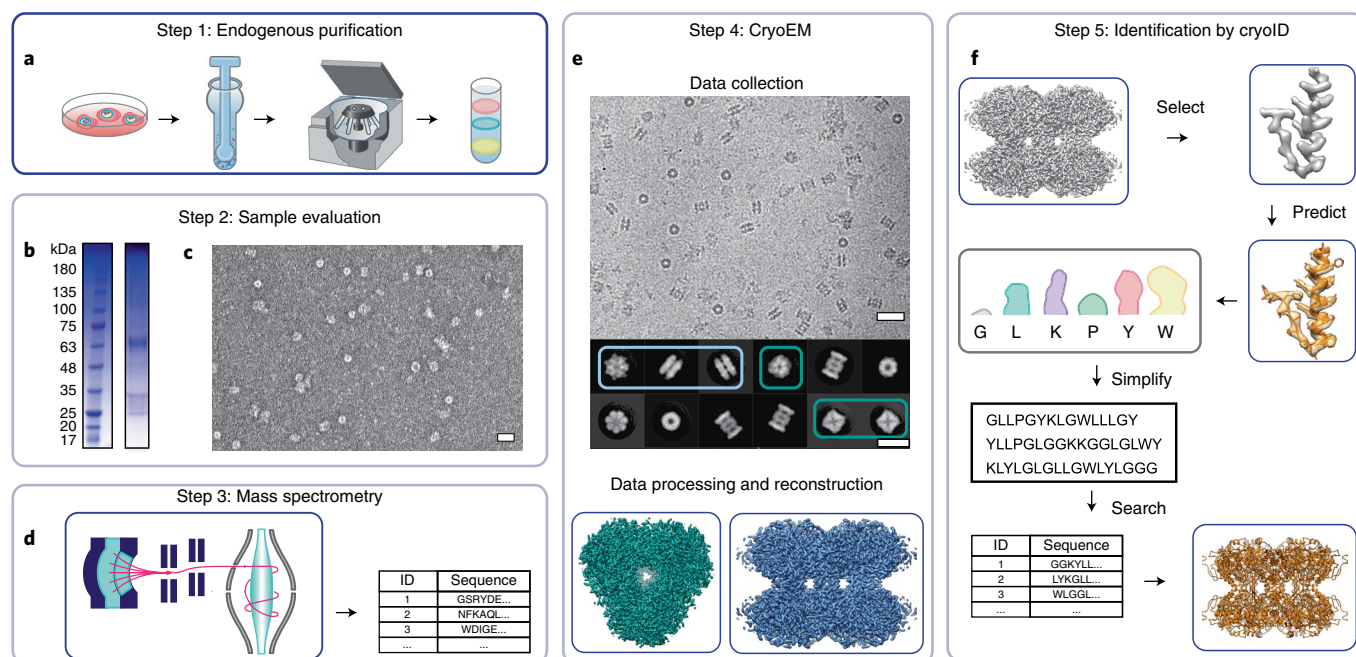


Fig. 1 | Endogenous structural proteomics workflow. **a**, Protein complexes are enriched by sucrose gradient fractionation. **b,c**, Fractions are evaluated by SDS-PAGE (**b**) and negative-stain electron microscopy (**c**), yielding a pool of all proteins present in each fraction, usually ~1,000–2,000 (Fig. 1d). **d**, Mass spectrometry identifies a list of all proteins in each fraction. **e**, cryoEM analysis yields near-atomic-resolution cryoEM maps. Scale bars, 30 nm (micrograph, top); 10 nm (2D class averages, bottom). **f**, The proteins in the cryoEM maps are identified using cryoID.

Step 3: Mass spectrometry. Promising fractions containing uniform particles in negative-stain EM (Supplementary Fig. 1) are analyzed by tryptic digestion liquid chromatography–mass spectrometry (LC–MS), yielding a pool of all proteins present in each fraction, usually ~1,000–2,000 (Fig. 1d).

Step 4: cryoEM imaging. Each promising fraction is imaged on a 300-kV cryo-electron microscope with a direct electron detector, generally yielding datasets containing several distinct protein complexes in each image (Fig. 1e). To deconvolute mixtures of several distinct protein complexes within a single dataset and resolve them into multiple three-dimensional (3D) structures, we leverage cryoSPARC's ability to perform unsupervised ab initio 3D classification and refinement⁷, given a mixture of particles from multiple distinct protein complexes.

Step 5: Protein identification and modeling. We have developed a semiautomated program, cryoID, which can identify the protein(s) in each cryoEM map obtained in Step 4, using only the cryoEM density, from the pool of potential candidates detected in the sample by mass spectrometry in Step 3 (Fig. 1f). As some amino-acid side chains can look quite similar in 3.0–4.0 Å cryoEM maps, we incorporated a certain degree of error tolerance into cryoID by introducing our new 'degenerate' 6-letter code that clusters the 20 amino-acid residues into 6 simplified groups on the basis of the similarity of their side-chain densities in typical cryoEM density maps (Fig. 2).

cryoID. cryoID, a key component of the above workflow, determines the unique identity of the protein(s) in a near-atomic-resolution (better than 4.0 Å) cryoEM density map from a pool of candidates (either full proteome(s) from Uniprot, or a list of possible proteins identified by mass spectrometry) using only the information contained within the cryoEM density map.

There are two main challenges in de novo modeling into cryoEM maps at 3.0–4.0 Å resolution, for both human modelers and automated modeling programs. The first is that distinguishability of

side-chain densities varies with map quality and local resolution(s), which can fluctuate widely across a cryoEM map. The second is that small and medium-size residues can be difficult to differentiate accurately, even in promising regions of the map, because their shapes are often less distinctive and can be context dependent. Aspartate and asparagine, for example, have side chains of a similar size and shape and are often difficult to distinguish without prior knowledge of the primary sequence.

We designed cryoID to emulate strategies used by human modelers in de novo model building to overcome these challenges (Supplementary Notes 1 and 2), resulting in a workflow consisting of four main tasks (Fig. 1f): selection, prediction, simplification and searching. Selection involves identifying high-resolution segments of the map with a continuous backbone and clearly distinguishable side-chain densities. For prediction, the polypeptide backbone for each map segment is automatically traced, and the identities of the side chains for each residue in the segment are semiautomatically predicted, yielding a predicted primary sequence for the segment. Simplification involves translating both the cryoEM map segment sequences and the pool of candidate protein sequences into our simplified six-letter code (Fig. 2). By using the six-letter code, we introduce a redundancy that imparts a degree of tolerance for errors made by cryoID during sequence prediction and eliminate the need for cryoID to differentiate between side chains of similar size and shape, which are often indistinguishable in typical cryoEM density maps. During the searching step, a customized BLASTP¹⁶ search of the entire pool of candidate proteins is performed using the previously predicted primary sequences for the cryoEM map segments as queries, yielding an expectation, or *E* value, that indicates the similarity between the query sequence and the candidate protein (Fig. 3). The *E* values for each query against a single candidate protein are combined to yield a composite *E* value, which indicates the likelihood of the candidate protein being the correct protein. These four tasks are accomplished by two cryoID subprograms, *get_queries* (selection and prediction) and *search_queries* (simplification and

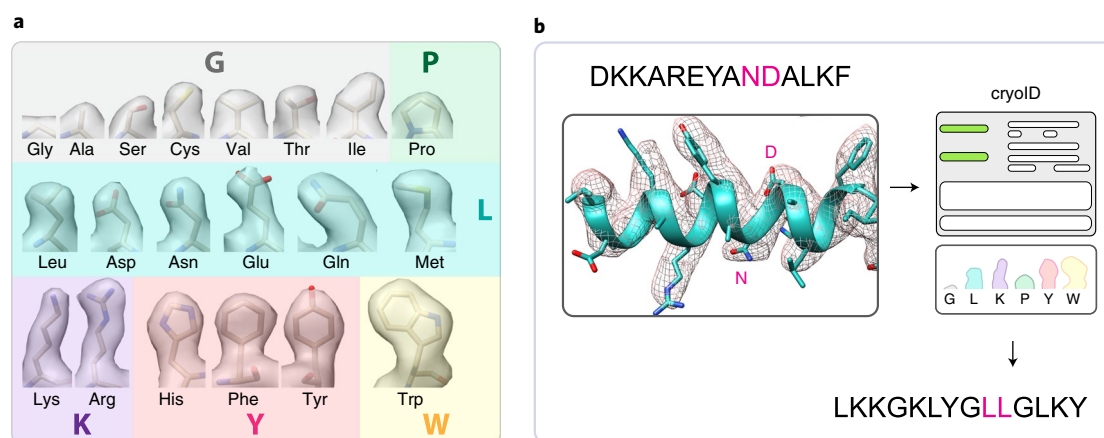


Fig. 2 | Simplified six-letter code. **a**, The 20 amino-acid residues are clustered into 6 simplified groups on the basis of the similarity of their side-chain densities in typical cryoEM density maps. One residue from each group is chosen as the representative of the entire group, denoted by the large colored single letter label in each group shown here (G group, small-size side-chain density; L group, medium-size side-chain density; K group, long and thin side-chain density; P group, typical proline side-chain density; Y group, long and bulky side-chain density). **b**, cryoID predicts the identity of each residue in the density on the left, and then simplifies the resulting sequence of the entire segment into the degenerate six-letter code shown on the right.

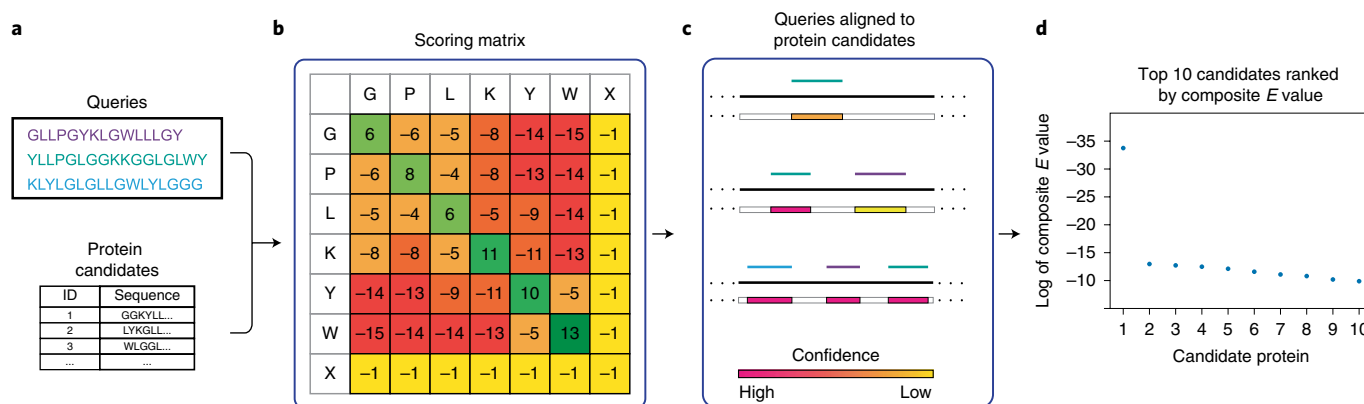


Fig. 3 | Searching in cryoID. **a**, cryoID runs alignments of the simplified query sequences obtained from the cryoEM maps against each protein in a pool of candidate proteins (also simplified). **b**, We created a customized alignment scoring matrix for cryoID by adapting the BLASTP PAM30 scoring matrix to work with the simplified six-letter code used by cryoID. **c,d**, cryoID calculates a composite *E* value for the alignment between each protein candidate against the query set, and then ranks the candidates by *E* value to determine the most likely match to the query set.

searching). Both subprograms can be executed automatically, with default parameters. Upon completion of the `get_queries` subprogram, cryoID launches the external visualization program Coot, which allows users to inspect, select and, if necessary, correct obvious mistakes (for example mistaking Gly for Arg) in the queries generated by `get_queries` (Supplementary Fig. 2). (This manual intervention could potentially be eliminated in the absence of obvious mistakes.)

We show, in a series of benchmarking experiments described below, that it is possible to uniquely identify the protein in a cryoEM map by using multiple simplified sequences of sufficient length from a single map to search a large pool (100–100,000) of candidates.

Benchmarking cryoID using simulated data. Parameters such as the number of queries, length of each query and number of errors in each query influence the ability of cryoID to arrive at a unique answer. We determined the optimal range for each parameter, using simulated datasets.

To determine the minimum number (*m*) of query sequences of a given length (*n*), from a single protein, required for cryoID to arrive at a unique answer, we varied *m* from 1–10 query sequences, and

n from 8–100 residues, as illustrated in Table 1. To cover a wide range of different sequences with varying amino-acid compositions and achieve a statistical significance ($P < 0.01$), we tested each condition (*m,n*) 1,000 times. To achieve this, we randomly generated multiple unique sets of queries from a full-length *P. falciparum* protein sequence for each condition (*m,n*), then used cryoID to simplify and search each set of queries against a pool of 880 full-length *P. falciparum* protein sequences, which were also simplified. For each set of queries, cryoID sorted protein candidates in the pool by their composite *E* values and monitored their percentage identity with the queries (Supplementary Fig. 3). We repeated this process with additional full-length *P. falciparum* proteins until we had tested 1,000 unique sets of queries for each condition (*m,n*).

Observing the efficacy of each combination of *m* and *n* from this simulated dataset allowed us to empirically determine the optimal query conditions (*m,n*) under which cryoID can correctly identify the unique protein matching the queries (Table 1). We defined optimal query conditions (*m,n*) as those for which cryoID consistently identified only a single protein that exhibited 100% identity with the queries (Supplementary Fig. 3b–d). For suboptimal query conditions (*m,n*) in which the query sequences were not long or

Table 1 | Determining optimal parameters for Searching in cryoID

Number of queries (<i>m</i>)	Query sequence length (<i>n</i>)														
	8	9	10	11	12	13	14	15	16	17	18	19	20	21	22
1	X	X	X	X	X	X	X	X	X	X	X	X	X	X	Y
2	X	X	X	X	X	X	X	Y	Y	Y	Y	Y	Y	Y	Y
3	X	X	X	Y	Y	Y	Y	Y	Y	Y	Y	Y	Y	Y	Y
4	X	X	Y	Y	Y	Y	Y	Y	Y	Y	Y	Y	Y	Y	Y
5	X	X	Y	Y	Y	Y	Y	Y	Y	Y	Y	Y	Y	Y	Y
6	X	Y	Y	Y	Y	Y	Y	Y	Y	Y	Y	Y	Y	Y	Y
7	Y	Y	Y	Y	Y	Y	Y	Y	Y	Y	Y	Y	Y	Y	Y
8	Y	Y	Y	Y	Y	Y	Y	Y	Y	Y	Y	Y	Y	Y	Y
9	Y	Y	Y	Y	Y	Y	Y	Y	Y	Y	Y	Y	Y	Y	Y
10	Y	Y	Y	Y	Y	Y	Y	Y	Y	Y	Y	Y	Y	Y	Y

The result for each query condition (*m,n*) shown here represents 1,000 tests of that condition using unique sets of queries randomly generated from full-length *P. falciparum* protein sequences. Conditions under which cryoID was consistently able to identify the correct protein are marked with Y. Conditions under which cryoID was unable to arrive at a single unique protein ID are marked with X. One-sided statistics test: $P(f) < 0.005$, $\bar{n} = 1,000$, P value < 0.0067 , $\alpha < 0.01$; where $P(f)$ = probability of failure to obtain unique protein ID.

numerous enough, cryoID identified multiple protein matches that exhibited 100% identity with the queries, making it impossible to obtain a unique protein ID (Table 1 and Supplementary Fig. 3a).

For cryoID runs under optimal query conditions (*m,n*), we observe that there is always a clear ‘gap’ in percentage identity between the correct protein candidate (100% identity with queries) and the next closest matching candidate (Supplementary Fig. 3b–d), which increases as *m* or *n* increases. This observation agrees with the theoretical estimation that, given a query set (*m,n*), the probability of achieving high identity with a candidate in the pool by chance can be approximated by $(1/6)^{m \times n}$. As such, the possibility of false-positive matches decreases exponentially as *m* and *n* increase. Therefore, we reasoned that it would still be possible for cryoID to determine a unique protein identification from queries containing a limited number of errors, provided that the number of errors remain less than the number of differences between the next closest matching candidate and the error-free queries.

By running each condition (*m,n*) enough times to achieve statistical significance ($\alpha < 0.01$), we empirically determined the minimum number of differences that can (probabilistically) occur between the correct protein and the next closest match in the pool, thus defining the maximum number of errors in a query set of (*m,n*) that cryoID can tolerate. We then used this information to predict the optimal conditions (*m,n*) for cryoID, given an incidence of 10%, 20%, 30% and 40% error in the queries.

These results are displayed in Supplementary Table 1, which serves as a reference table for deciding the optimal number and length of queries users should aim for. The table describes the minimum average query length (*n*) required for cryoID to identify the correct protein using a given number of queries (*m*), as well as the maximum percentage of errors that can be tolerated for each query condition (*m,n*). The table is based on our protein candidate pool, containing 880 proteins (~750,000 amino-acid residues).

Validation of cryoID using published cryoEM maps from the EMDB. Having determined the optimal range for each parameter using simulated datasets, we then tested cryoID against published experimental cryoEM maps available from the Electron Microscopy Data Bank (EMDB), following our workflow detailed in Fig. 1f.

We selected two published cryoEM structures within our target resolution range (3.0–4.0 Å) from the EMDB, a 3.4 Å structure of human gamma-secretase (EMD-3061)¹⁷, and a 3.6 Å structure of the *Drosophila melanogaster* NOMPC mechanotransduction

channel (EMD-8702)¹⁸. Gamma-secretase is a four-membered intramembrane protease consisting of presenilin, presenilin enhancer 2 (PEN-2), nicastrin and anterior pharynx-defective 1 (APH-1). NOMPC is a homotetrameric integral membrane protein. We analyzed each map in cryoID, generating a single query set for NOMPC, and two separate query sets for the cytosolic and transmembrane regions of gamma-secretase. cryoID successfully identified the correct protein in the NOMPC map from both a more limited candidate pool consisting of the 3,500 proteins in the *D. melanogaster* proteome, as well as a much larger candidate pool containing all ~560,000 reviewed proteins in the UniProt database (Supplementary Table 2). cryoID also successfully identified the correct proteins in both regions of the human gamma-secretase map from which we generated query sets, from both a candidate pool consisting of the 20,397 proteins in the *H. sapiens* proteome, as well as against the entire ~560,000 reviewed proteins in the UniProt database (Supplementary Tables 3 and 4). For regions of the map corresponding to the other 2 components of gamma-secretase, cryoID generated 1–2 short queries that were insufficient for unambiguous identification of the corresponding component owing to poor map quality. In partial identification cases like this, it is likely that these queries belong to an unidentified component of the complex that is flexibly attached, and only the region that is anchored firmly to the complex is resolved to high resolution. If the flexibly attached component is ordered, performing focused classification and refinement techniques to improve the local resolution of the cryoEM map in this region before applying cryoID to identify the unknown component may help. Indeed, in the case of human gamma-secretase, applying cryoID to subsequently improved cryoEM maps¹⁹ yielded the successful identification of the previously unidentified components. If this approach fails, the flexibly attached component may be intrinsically disordered. In this case, the pool of potential candidates can be narrowed down to a short-list consisting only of proteins that contain intrinsically disordered domains and are known to interact with the components of the complex previously identified by cryoID.

Thus, using published cryoEM maps from the EMDB, we determined that cryoID can consistently determine the correct protein(s) in cryoEM maps from entire proteomes, ranging anywhere from 1000–20,000 proteins in size. We further found that for the 2 published cryoEM maps used here, cryoID was capable of identifying the correct protein(s) from a much larger candidate pool consisting of the entire ~560,000 proteins in the UniProt database.

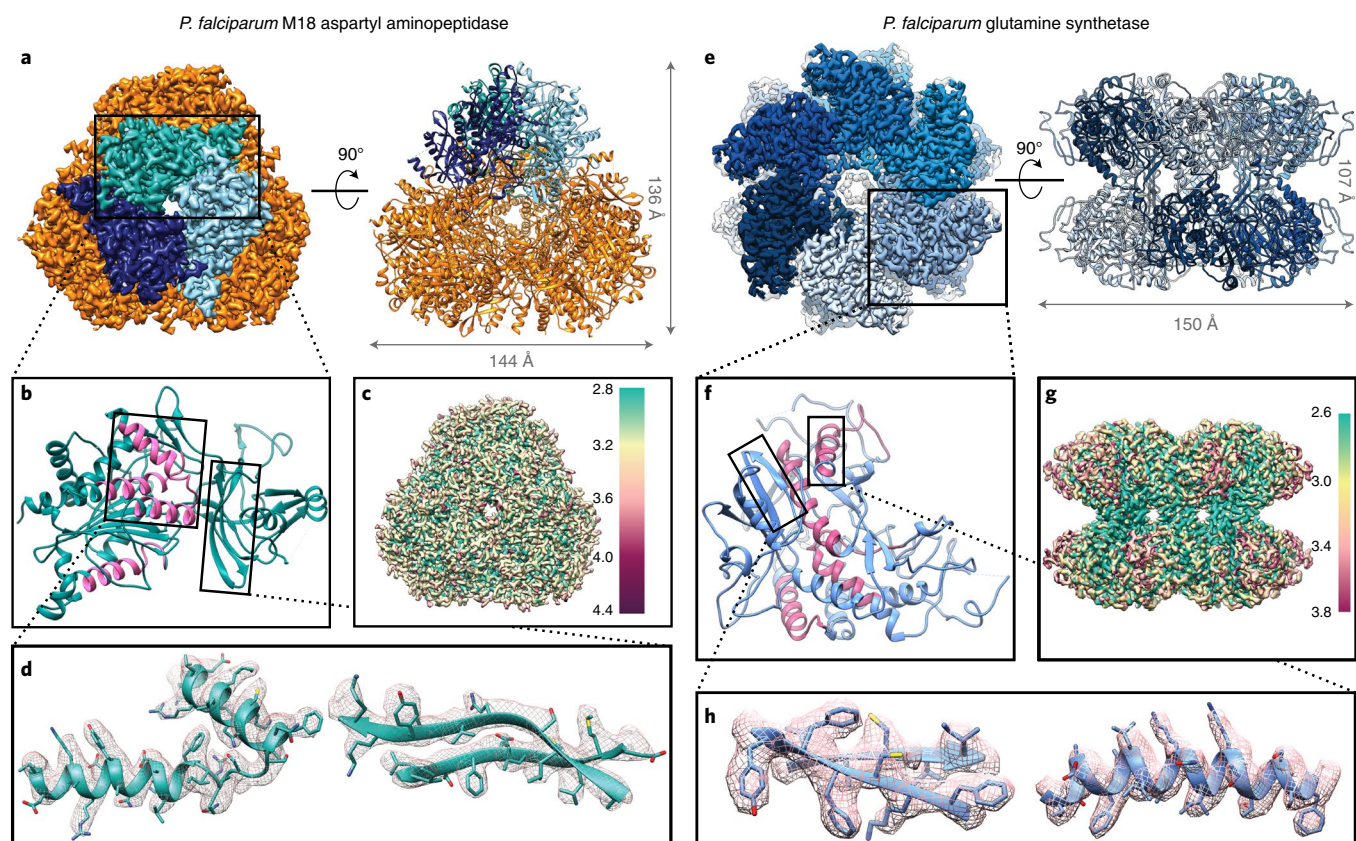


Fig. 4 | CryoEM structures of proteins enriched directly from *P. falciparum* parasite lysates. a,e, 3.2-Å cryoEM density map and atomic model of *P. falciparum* M18 aspartyl aminopeptidase (**a**) and glutamine synthetase (**e**). **b,f**, Enlarged view of the *P. falciparum* M18 aspartyl aminopeptidase (**b**) and glutamine synthetase (**f**) monomer. Segments from which the queries for cryoID were generated are highlighted in pink. **c,g**, Local resolution (in Å) calculated using Resmap and two unfiltered halves of the reconstruction for *P. falciparum* M18 aspartyl aminopeptidase (**c**) and glutamine synthetase (**g**). **d,h**, Detailed view of regions boxed in **b** and **f**, displayed with corresponding cryoEM density.

Application of endogenous structural proteomics workflow to *P. falciparum*. We used the challenging organism *P. falciparum* to further test the ability of our entire workflow to yield near-atomic-resolution structures of protein complexes enriched directly from endogenous sources. Many pathogens of high medical relevance are recalcitrant to structural characterization using traditional recombinant approaches. This is particularly so in the case of *P. falciparum*, for which the paucity of high-resolution structural and functional information is compounded by the fact that ~50% of the *P. falciparum* proteome is novel^{20–22} and bears no similarity to existing structures in the PDB. Many of the most promising *P. falciparum* drug targets are membrane proteins, but there are only two unique integral membrane protein structures from *P. falciparum* in the PDB^{10,23}.

We enriched for protein complexes ranging from 100 kDa to ≥ 2.0 MDa from *P. falciparum* NF54 parasite lysate using sucrose gradient fractionation. Analysis of a single cryoEM dataset collected from the fraction that looked the most promising by SDS-PAGE and negative-stain EM (Supplementary Fig. 1) yielded multiple near-atomic-resolution cryoEM density maps at an overall resolution ranging from 3.2–3.6 Å, including two unknown protein complexes, as well as two distinct conformations of the 20S proteasome that exhibit marked differences from the previously published *P. falciparum* 20S proteasome structure^{24,25} (Fig. 4, Supplementary Fig. 4). Mass spectrometry identified a candidate pool of 773 proteins in the fraction (Supplementary Table 5).

We analyzed each of the unknown maps in cryoID following the workflow detailed in Fig. 1f, generating a single query set per map. In each case, cryoID successfully identified the correct protein in

the map from the candidate pool, enabling us to build atomic models of the two protein complexes.

Cross-validation against pre-existing crystal structure of the *P. falciparum* M18 aspartyl aminopeptidase. The protein in the first 3.2-Å cryoEM map was identified to be *P. falciparum* M18 aspartyl aminopeptidase, a 788-kDa homo-dodecameric complex with tetrahedral symmetry (Fig. 4a, Supplementary Table 6 and Supplementary Video 1). Our de novo structure agrees extremely well with the previously reported X-ray crystallographic structure of this complex²⁶ (Fig. 5a), with both the regulatory (amino-acid residues 1–92 and 307–577) and catalytic (residues 92–306) domains clearly visible in all subunits (Fig. 5b). As such, the previously published crystal structure serves as a gold standard validation of our method.

Structure of *P. falciparum* glutamine synthetase reveals new structural features unique to *Plasmodium*. The protein in the second 3.2-Å cryoEM map was identified to be *P. falciparum* glutamine synthetase, a 759-kDa homo-dodecameric complex which adopts a two-tiered ring shape with D6 symmetry (Fig. 4e, Supplementary Table 7 and Supplementary Video 2). This enzyme catalyzes the condensation of glutamate and ammonia into glutamine in an ATP-dependent manner. The active site, positioned between adjacent monomers, contains binding sites for ATP, glutamate, and ammonia, as well as two pockets for the binding of divalent cations (either Mg²⁺ or Mn²⁺)²⁷.

Our de novo atomic model from the cryoEM map is similar throughout most of the structure (root-mean-squared deviation,

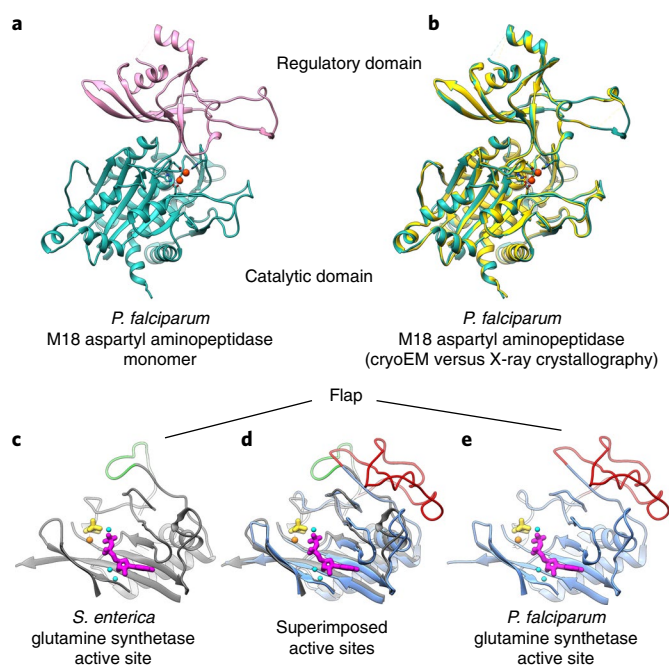


Fig. 5 | Details of the M18 aspartyl aminopeptidase and glutamine synthetase monomers. **a**, A single monomer from our atomic model of the *P. falciparum* M18 aspartyl aminopeptidase (*P. falciparum* M18AAP), solved by cryoEM using our endogenous structural proteomics workflow, colored to indicate the regulatory (pink) and catalytic (sea green) domains. **b**, Our atomic model of *P. falciparum* M18AAP (sea green), solved by cryoEM using our endogenous structural proteomics workflow, is shown superimposed with the previously published structure of *P. falciparum* M18AAP (gold), solved using X-ray crystallography. The structures align with a root-mean-square deviation (RMSD) of 0.548 Å. **c**, The previously published structure of the *S. enterica* glutamine synthetase, solved using X-ray crystallography, colored dark grey. **d**, Our cryoEM structure of the *P. falciparum* glutamine synthetase, colored cornflower blue, is shown superimposed with the *S. enterica* glutamine synthetase crystallographic structure. The two structures align with an RMSD of 1.5 Å. **e**, A single monomer from our atomic model of the *P. falciparum* glutamine synthetase, determined by cryoEM using our endogenous structural proteomics workflow, colored in cornflower blue. We observed an extra 50-residue insertion in the *P. falciparum* structure (colored red) that is absent in the *S. enterica* structure. This long insertion forms a large flap that curls away from the active site, unlike the shorter flap formed by the corresponding region in the *S. enterica* glutamine synthetase (colored green), which curls toward the active site.

RMSD = 1.5 Å) to the previously published atomic model of a close homolog from *S. enterica*, solved by X-ray crystallography to 2.67-Å resolution²⁸ (Supplementary Fig. 5). In particular, the three substrate-binding pockets in the active site are well conserved (Fig. 5c–e).

However, we do observe one major difference between the two structures (Fig. 5c–e). In the *S. enterica* structure, residues 393–410 form a short loop shaped like a flap that folds partially across the entrance to the active site (Fig. 5c). In the corresponding location in our structure from *P. falciparum*, there is an extra 50-residue insertion here that forms a long loop that folds down along the outside of the structure, in the opposite direction from the active site (Fig. 5e).

Structures of *P. falciparum* 20S proteasome reveal new conformational states. Analysis of the most abundant particles in our dataset yielded 2 distinct cryoEM maps at 3.48 Å and 3.67 Å which cryoID successfully identified to be the *P. falciparum* 20S proteasome in 2 distinct conformations (Supplementary Fig. 4). All 28 subunits were well-resolved in the 3.48 Å structure of the first conformation.

However, the $\beta 4$ and $\beta 5$ subunits in the 3.67-Å structure of the second conformation are disordered, and thus are visible only when the map is filtered to lower resolution, suggesting that these subunits are flexible (Supplementary Fig. 4g,h). As such, we named this second structure the 20S proteasome- $\beta 4\beta 5_{\text{flex}}$. Comparison of our structures with the previously published *P. falciparum* 20S proteasome structure^{24,25} revealed considerable differences in both of our new structures, the most striking of which is the disordered $\beta 4$ and $\beta 5$ subunits in the 20S proteasome- $\beta 4\beta 5_{\text{flex}}$ conformation structure.

Discussion

We present a new cryoEM pipeline for obtaining near-atomic-resolution structures of native, untagged protein complexes enriched directly from endogenous sources. cryoID, an essential component of the workflow, successfully identifies protein(s) in better than 4.0-Å-resolution cryoEM maps of protein complexes, without prior knowledge of primary sequence(s). As a proof of principle, we used this pipeline to obtain near-atomic-resolution structures of multiple protein complexes enriched directly from unmodified *P. falciparum* parasites.

The holy grail of structural biology is to determine atomic structures for the entire proteome of a living cell without disrupting the macromolecular complexes from their native environment—commonly referred to as in situ structural biology^{29,30}. The current state-of-the-art method for direct visualization of biological structures in vivo involves cryo electron tomographic (cryoET) imaging and reconstruction of thin sections, called lamella, of intact cells, created using a focused ion-beam scanning electron microscope (FIB-SEM)^{31–33}. Although cryoFIB milling can be used to overcome the fundamental limitation in the thickness of samples amenable to imaging by cryoET, both cryoET and cryoFIB milling are laborious, technically challenging, and far from routine at the present time, typically yielding at most 10 lamellae per day, each encompassing a mere 1–2 μm^2 of imageable area per cell. As such, obtaining enough lamella tomograms to accumulate the 100,000–500,00 particles of a macromolecular complex needed to achieve near-atomic resolution is currently impractical.

The bottom-up endogenous structural proteomics approach presented here is broadly applicable and represents an immediate step toward direct visualization of native protein complexes as they exist in the cellular milieu at near-atomic resolution. Notwithstanding the challenges posed by low abundance or flexible species, our approach opens the door for structural study of endogenous protein complexes from an enormous number of organisms that have yet to be fully explored, enabling direct observation at near-atomic resolution of previously unidentified novel protein complexes captured in multiple native conformational states (for example, changes in binding partners or cycling through subcomplexes like the spliceosome^{34–40}) and during various stages of biological processes (for example, parasite life cycles, progression of cancers or cardiovascular diseases).

Online content

Any methods, additional references, Nature Research reporting summaries, source data, extended data, supplementary information, acknowledgements, peer review information, details of author contributions and competing interests, and statements of code and data availability are available at <https://doi.org/10.1038/s41592-019-0637-y>.

Received: 30 January 2019; Accepted: 7 October 2019;

Published online: 25 November 2019

References

- Cheng, Y. Single-particle cryo-EM at crystallographic resolution. *Cell* **161**, 450–457 (2015).

2. Li, X. et al. Electron counting and beam-induced motion correction enable near-atomic-resolution single-particle cryo-EM. *Nat. Methods* **10**, 584–590 (2013).
3. Liu, H. et al. Atomic structure of human adenovirus by cryo-EM reveals interactions among protein networks. *Science* **329**, 1038–1043 (2010).
4. McMullan, G., Chen, S., Henderson, R. & Faruqi, A. R. Detective quantum efficiency of electron area detectors in electron microscopy. *Ultramicroscopy* **109**, 1126–1143 (2009).
5. Clough, G. M. R. N. & Kirkland, A. I. in *Journal of Physics: Conference Series* Vol. 522 (IOP Publishing, 2013).
6. Zhang, X., Jin, L., Fang, Q., Hui, W. H. & Zhou, Z. H. 3.3 A cryo-EM structure of a nonenveloped virus reveals a priming mechanism for cell entry. *Cell* **141**, 472–482 (2010).
7. Punjani, A., Rubinstein, J. L., Fleet, D. J. & Brubaker, M. A. cryoSPARC: algorithms for rapid unsupervised cryo-EM structure determination. *Nat. Methods* **14**, 290–296 (2017).
8. Scheres, S. H. W. A bayesian view on cryo-EM structure determination. *J. Mol. Biol.* **415**, 406–418 (2012).
9. Scheres, S. H. W. RELION: implementation of a bayesian approach to cryo-EM structure determination. *J. Struct. Biol.* **180**, 519–530 (2012).
10. Ho, C. M. et al. Malaria parasite translocon structure and mechanism of effector export. *Nature* **561**, 70–75 (2018).
11. Niedzialkowska, E. et al. Protein purification and crystallization artifacts: the tale usually not told. *Protein Sci.* **25**, 720–733 (2016).
12. Osipiuk, J., Walsh, M. A. & Joachimiak, A. Crystal structure of MboIIA methyltransferase. *Nucleic Acids Res.* **31**, 5440–5448 (2003).
13. Adams, P. D. et al. PHENIX: a comprehensive Python-based system for macromolecular structure solution. *Acta Crystallogr. D* **66**, 213–221 (2010).
14. Porebski, P. J., Cymborowski, M., Pasenkiewicz-Gierula, M. & Minor, W. Fitmunk: improving protein structures by accurate, automatic modeling of side-chain conformations. *Acta Crystallogr. D Biol.* **72**, 266–280 (2016).
15. PDB statistics: overall growth of released structures per year, <https://www.rcsb.org/stats/growth/overall> (2018).
16. Altschul, S. F., Gish, W., Miller, W., Myers, E. W. & Lipman, D. J. Basic local alignment search tool. *J. Mol. Biol.* **215**, 403–410 (1990).
17. Bai, X. C. et al. An atomic structure of human gamma-secretase. *Nature* **525**, 212–217 (2015).
18. Jin, P. et al. Electron cryo-microscopy structure of the mechanotransduction channel NOMPC. *Nature* **547**, 118–122 (2017).
19. Zhou, R. et al. Recognition of the amyloid precursor protein by human gamma-secretase. *Science* **363**, eaaw0930 (2019).
20. Gardner, M. J. et al. Genome sequence of the human malaria parasite *Plasmodium falciparum*. *Nature* **419**, 498–511 (2002).
21. Hall, N. et al. A comprehensive survey of the plasmodium life cycle by genomic, transcriptomic, and proteomic analyses. *Science* **307**, 82–86 (2005).
22. Waters, A. P. Genome-informed contributions to malaria therapies: feeding somewhere down the (pipe)line. *Cell Host Microbe* **3**, 280–283 (2008).
23. Newby, Z. E. et al. Crystal structure of the aquaglyceroporin PfAQP from the malarial parasite *Plasmodium falciparum*. *Nat. Struct. Mol. Biol.* **15**, 619–625 (2008).
24. Li, H. et al. Structure- and function-based design of *Plasmodium*-selective proteasome inhibitors. *Nature* **530**, 233–236 (2016).
25. Xie, S. C. et al. The structure of the PA28-20S proteasome complex from *Plasmodium falciparum* and implications for proteostasis. *Nat. Microbiol.* **4**, 1990–2000 (2019).
26. Sivaraman, K. K. et al. X-ray crystal structure and specificity of the *Plasmodium falciparum* malaria aminopeptidase PfM18AAP. *J. Mol. Biol.* **422**, 495–507 (2012).
27. Eisenberg, D., Gill, H. S., Pfluegl, G. M. & Rotstein, S. H. Structure-function relationships of glutamine synthetases. *Biochim. Biophys. Acta* **1477**, 122–145 (2000).
28. Gill, H. S. & Eisenberg, D. The crystal structure of phosphinothricin in the active site of glutamine synthetase illuminates the mechanism of enzymatic inhibition. *Biochem.-Us* **40**, 1903–1912 (2001).
29. Asano, S., Engel, B. D. & Baumeister, W. In situ cryo-electron tomography: a post-reductionist approach to structural biology. *J. Mol. Biol.* **428**, 332–343 (2016).
30. Beck, M. & Baumeister, W. Cryo-Electron tomography: can it reveal the molecular sociology of cells in atomic detail? *Trends Cell Biol.* **26**, 825–837 (2016).
31. Albert, S. et al. Proteasomes tether to two distinct sites at the nuclear pore complex. *Proc. Natl. Acad. Sci. USA* **114**, 13726–13731 (2017).
32. Mahamid, J. et al. Visualizing the molecular sociology at the HeLa cell nuclear periphery. *Science* **351**, 969–972 (2016).
33. Mosalaganti, S. et al. In situ architecture of the algal nuclear pore complex. *Nat. Commun.* **9**, 2361 (2018).
34. Bai, R., Wan, R., Yan, C., Lei, J. & Shi, Y. Structures of the fully assembled *saccharomyces cerevisiae* spliceosome before activation. *Science* **360**, 1423–1429 (2018).
35. Zhang, X. et al. Structures of the human spliceosomes before and after release of the ligated exon. *Cell Res.* **29**, 274–285 (2019).
36. Liu, S. et al. Structure of the yeast spliceosomal postcatalytic P complex. *Science* **358**, 1278–1283 (2017).
37. Agafonov, D. E. et al. Molecular architecture of the human U4/U6.U5 tri-snRNP. *Science* **351**, 1416–1420 (2016).
38. Galej, W. P. et al. Cryo-EM structure of the spliceosome immediately after branching. *Nature* **537**, 197–201 (2016).
39. Haselbach, D. et al. Structure and conformational dynamics of the human spliceosomal B(act) complex. *Cell* **172**, 454–464 e411 (2018).
40. Nguyen, T. H. D. et al. Cryo-EM structure of the yeast U4/U6.U5 tri-snRNP at 3.7 Å resolution. *Nature* **530**, 298–302 (2016).

Publisher's note Springer Nature remains neutral with regard to jurisdictional claims in published maps and institutional affiliations.

© The Author(s), under exclusive licence to Springer Nature America, Inc. 2019

Methods

Parasite culture. *P. falciparum* cultures were prepared as described previously¹⁰.

Sucrose gradient fractionation of *P. falciparum* parasite lysate. Frozen parasite pellets were resuspended in Lysis Buffer (25 mM HEPES pH 7.4, 10 mM MgCl₂, 150 mM KCl, 10% glycerol) and homogenized using a glass Dounce tissue homogenizer. The cytosolic fraction was isolated from the homogenized lysate by centrifugation at 100,000g for 1 h. The soluble lysate was then fractionated with a 15–40% sucrose gradient.

The presence and relative abundance of large protein complexes of interest were ascertained by silver-stained SDS–PAGE and tryptic digestion LC–MS (Supplementary Table 5). The extremely low yields that are achievable when purifying protein complexes directly from *P. falciparum* parasites prohibited the conventional approach of evaluating sample quality by size-exclusion chromatography. Thus, during the iterative process of screening for fractions containing complexes of interest as well as optimal fractionation conditions, sample quality was assessed by negative-stain (uranyl acetate) transmission electron microscopy in an FEI TF20 microscope equipped with a TVIPS 16 megapixel charge-coupled device (CCD) camera. Briefly, small datasets of ~100,000 particles were collected, and 2D class averages were generated in RELION^{8,9} to assess the presence of sufficient numbers of intact particles yielding class averages exhibiting distinct features. For example, various symmetries could be recognized in top and side views (Fig. 1e and Supplementary Fig. 1e).

Mass spectrometry. Selected fractions of interest were digested using trypsin, as previously described⁴¹. Digested samples were then fractionated online using reverse-phase chromatography and were analyzed by tandem mass spectrometry on a Q-Exactive mass spectrometer⁴². Data were analyzed on the IP2 software platform, which utilizes ProLuCID for database searching and DTASelect for filtering with decoy-database-estimated false-discovery rates^{43,44}. The proteomics data have been deposited to the ProteomeXchange Consortium (<http://proteomecentral.proteomexchange.org>) via the MassIVE partner repository with the dataset identifier PDX014263.

cryoEM. 3- μ l aliquots of fractionated lysate were applied to glow-discharged lacey carbon grids with a supporting ultrathin carbon film (Ted Pella). Grids were then blotted with filter paper and vitrified in liquid ethane using an FEI VitroBot Mark IV. CryoEM grids were screened in an FEI Tecnai TF20 transmission electron microscope to optimize freezing conditions.

Higher resolution cryoEM images were collected on a Gatan K2-Summit direct electron detector in super-resolution electron counting mode on an FEI Titan Krios at 300 kV equipped with a Gatan Quantum energy filter set at a 20-eV slit width. Fifty frames were recorded for each movie at a pixel size of 1.07 Å at the specimen scale, with a 200-ms exposure time and an average dose rate of 1.2 electrons per Å² per frame, resulting in a total dose of 60 electrons per Å² per movie. The final dataset consists of a total of 2,514 movies.

Image processing and 3D reconstruction. Frames in each movie were aligned, gain reference-corrected and dose-weighted to generate a micrograph using MotionCor2 (ref. ⁴⁵). Aligned and un-dose-weighted micrographs were also generated and used for contrast transfer function (CTF) estimation using CTFFIND4 (ref. ⁴⁶), for particle picking by hand, and for particle picking using Gautamatch⁴⁷.

328,435 particles were extracted from 2,514 micrographs. After several rounds of reference-free 2D classification in RELION, junk particles were excluded. 47,159 particles belonged to good 2D class averages that exhibited clear secondary structure features and resembled typical²⁴ 20S proteasome top and side views. On finer classification, two distinct side views and two distinct top views emerged, suggesting the presence of multiple native conformations. All 47,159 particles were subjected to an unsupervised single-class ab initio 3D reconstruction followed by a two-class heterogeneous refinement using C1 symmetry in CryoSPARC. The resulting two reconstructions were then individually subjected to homogenous refinement using C2 symmetry in CryoSPARC, yielding two distinct structures at a final overall resolution of 3.48 Å (from 24,788 particles) and 3.67 Å (from 16,588 particles), respectively (Supplementary Fig. 4).

22,596 particles belonging to good 2D class averages that exhibited clear secondary structure features but did not resemble proteasomes were then used in an unsupervised four-class ab initio 3D reconstruction followed by separate homogeneous refinements in CryoSPARC⁷, yielding two 3.2 Å ab initio 3D maps.

Further refinement of the particles in any of the four above mentioned structures in RELION failed to yield any improvement in resolution.

Manual model building and refinement. Map interpretation was performed with UCSF Chimera⁴⁸ and COOT⁴⁹. *P. falciparum* protein sequences were obtained from the National Center for Biotechnology Information (NCBI)⁵⁰ and the PlasmoDB⁵¹ protein databases. Sequence registration during model building of *P. falciparum* glutamine synthetase and *P. falciparum* M18 aspartyl aminopeptidase was guided by reference to homologs (accession codes 1FPY and 4EME, respectively) as well as PHYRE2 (ref. ⁵²) secondary structure predictions. For the M18 aspartyl

aminopeptidase structure, each residue in the monomer was manually refit in COOT to optimize geometry and fit. For the glutamine-synthetase structure, each residue in the monomer was manually traced and built de novo in COOT. The model of the monomer for each protein was then propagated to match the biological assembly and rigid-body fit into the density map.

Manual refinement targeting both protein geometry and fit with the density map was used primarily in the core regions where resolution was higher and noise was minimal. To improve the geometry and fit, manual adjustments were made to protein geometry and density-map fit, using Molprobity⁵³ clash dots and sphere-refinement in COOT. Rotamers were fit manually in COOT and improved using the 'Back-rub Rotamers' setting. The resulting models for the complexes were subjected to the phenix.real_space_refine program in PHENIX¹³.

All figures and videos were prepared with UCSF Chimera, Pymol⁵⁴ and Resmap⁵⁵. Molprobity was used to validate the stereochemistry of the final models.

Building cryoID. We developed the Python-based cryoID program (Fig. 1f) using the scientific Python development environment Spyder. cryoID consists of two main subprograms, `get_queries` and `search_pool`. The subprogram `get_queries` performs the selection and prediction functionalities of cryoID, identifying one or more high-resolution segments of the map with a continuous backbone and clearly distinguishable side-chain densities. It then automatically traces the polypeptide backbone for each map segment and semiautomatically predicts the identities of the side chains for each residue in the segment, yielding a predicted primary sequence for the segment. The subprogram `search_pool` performs the simplification and search functionalities of cryoID, translating both the cryoEM map-segment sequences (that is, queries) and all the primary sequences of the pool of candidate proteins into a simplified six-letter code and performing a modified blast search of the entire pool of candidate proteins using the predicted cryoEM map segment sequences as queries. Both `get_queries` and `search_pool` subprograms of cryoID are detailed below.

We also developed a graphical user interface (GUI) for cryoID using the cross-platform Qt GUI toolkit and its Python binding, PyQt. The two subprograms can be accessed either via the GUI, or from the command line. cryoID is an open-source program under the MIT license, available for download at github (<https://github.com/EICN-UCLA/cryoID>).

Selection and prediction using `get_queries`. The first cryoID subprogram, `get_queries`, generates multiple query sequences from the cryoEM density map. cryoID automatically assesses the backbone continuity when generating queries in the following manner: cryoID calls the `sequence_from_map` function in the *Phenix* software package, which automatically builds a model, typically composed of many fragments, into the cryoEM density. First, regular secondary structure (helices, strands) are identified. Then, the contour level in the map is initially set to a very high level and is gradually lowered until connections appear between the secondary-structure elements. If branching occurs, the process is stopped. This procedure defines the connectivity of a fragment and its ends. Once a fragment is identified, the chain is traced through it by following high density. Ca/C β positions are identified from bumps extending from the main chain in the density, and an all-atom model is constructed using Pulchra⁵⁶ (an existing fast all-atom reconstruction algorithm). Only the longest fragments are considered in the consequent sequence prediction and analysis (typically 15–50 amino-acid residues in length). At each residue in each fragment, the most likely amino acid is identified by comparison of side-chain density in the cryoEM map at this position with a library of side-chain densities extracted from a large set of cryoEM maps and models. This results in a predicted sequence for each fragment.

Upon completion, two files are generated: a FASTA file containing the query sequences and a corresponding .pdb file containing the atomic coordinates for each sequence.

`get_queries` then calls COOT to open the density map with the .pdb file for user inspection, and if necessary, manual deletion of poor segment sequences, and correction of incorrectly assigned residues to the right group (Supplementary Fig. 2) and unidentifiable residues to 'X' (which is designated with the residue type 'MSE') using the 'mutate residue' tool in COOT. The modified .pdb file is then saved and passed on to the second cryoID subprogram as the query set. Experienced users can also directly modify the sequences in the FASTA file, using the segment density as a reference.

The `get_queries` subprogram requires three user-provided inputs: the cryoEM density map filename, high resolution limit for map analysis, and symmetry of the cryoEM density map, which can be provided either from our GUI or from the command line. For the resolution parameter, one may start with the average global resolution reported by reconstruction programs and then fine-tune this parameter on the basis of the estimated local resolution of the selected regions. The `get_queries` subprogram should complete relatively quickly, generally within 1 h, depending on factors such as map size and symmetry. For reference, processing of the glutamine synthetase and M18 aspartyl aminopeptidase maps was completed in 5–10 min, while processing of the NOMPC and human gamma-secretase maps were completed in ~50 min on a single CPU core. The version of Phenix utilized by cryoID in all the benchmarking results was Phenix-1.14-3260.

Simplification and searching using search_pool. The second cryoID subprogram, search_pool, performs alignments of the query sets generated by the get_queries cryoID subprogram against the full-length protein sequences of all the proteins in a user-defined candidate protein pool. The program requires two inputs: (1) a file containing a list of query sequences in either standard fasta format or in the .pdb format generated by the get_queries cryoID subprogram (in the latter case, the sequence information is extracted by calling PHENIX.print_sequence in the search_pool subprogram); (2) a FASTA file containing a list of the proteins in the user-defined candidate protein pool. The search_pool subprogram then translates both the query and candidate sequences into the simplified six-letter code (Fig. 2a).

Once this is accomplished, the search_pool subprogram calls the widely distributed local alignment search tool BLASTP¹⁶ to search the candidate protein pool for the protein that contains segments matching the query sequences. In preparation for the BLASTP search, the program first generates a local database from the degenerate candidate protein sequences with makeblastdb. The codes for the six degenerate categories are selected (G-like → G, P-like → P, L-like → Z, K-like → M, Y-like → Y, W-like → W) on the basis of the PAM30 scoring matrix so that the substitution scoring matrix used has higher bonus scores for matches to P-like/K-like/Y-like/W-like categories and appropriate penalty scores for mismatches depending on the severity of side-chain shape dissimilarity (between categories (Fig. 3b)). By default, the program prohibits gapped alignments (insertions/deletions) during BLASTP search by setting very high penalty scores for gap open (−32,767) and gap extension (−32,767). Experienced users may take advantage of additional arguments through the advanced option input in the GUI. For example, users can choose to include gapped alignments during the BLASTP search by adjusting the penalty scores.

For each of the query sequences, the program calls a BLASTP search. The following arguments are used for each search to optimize the BLASTP search for short degenerate sequences: -task blastp-short -matrix PAM30 -db/database/dbname -query query_file -out output_name -eval 1 -comp_based_stats F -dbsize dbsize -searchsp searchsp -word_size 2 -gapopen 32767 -gapextend 32767 -outfmt 7, where dbsize/searchsp specifies the effective size of the database/search space (in our case, we use the actual size). If the polarity of the query sequence (that is, amino/carboxy termini) is unknown, users can add a 'polarity unknown' flag (-r) in the GUI options so that the program will try to align the query against the protein pool in both polarities. Each search generates a list of sequence segments belonging to the protein candidate pool that match the query with alignment statistics (such as alignment length, percentage identity, *E* value, number of mismatches, and so on). The program then evaluates these matched sequences on the basis of the alignment length and *E* value: those with very short length (<60% of the query length) are discarded, and for each matched protein, the one with the smallest *E* value is selected.

For each matched protein, the program quantifies the quality of the match by calculating a composite *E* value of the search results of all queries, as defined below:

$$E_{i,j} = \prod_{j=1}^N (\min(E_{i,j}, 1) \times l_i)$$

where *i* is the *i*th protein, *j* the *j*th query, *N* the number of queries, *E_{i,j}* the *E* value of the *i*th protein for query *j*, and *l* length factor (that is, length / 1,000) of the *i*th protein.

Finally, the program sorts all matched proteins based on the composite *E* value, and the resulting list is saved in a summary file. The protein candidate with the smallest composite *E* value is on the top of the list and should correspond to the correct protein, provided that the queries satisfy the rules as outlined in Supplementary Table 1.

In rare instances where the query contains too many errors, the queries are too few, or the length too short, the matched protein with the smallest composite *E* value is a false positive. False-positive matches can be readily recognized either during model building or if their abundance in the mass spectrometry results do not agree with their contribution to the particle population in the cryoEM images.

Benchmarking on published structures. We tested cryoID against two published experimental cryoEM maps available for the EMDB, the human gamma-secretase (3.4 Å) and the *D. melanogaster* mechanotransduction channel NOMPC, which have global resolutions in our target resolution range (better than 4.0 Å).

cryoID and human gamma-secretase. Human gamma-secretase is a four-membered intramembrane protease consisting of presenilin, PEN-2, nicastrin and APH-1. We tested get_queries for on the human gamma-secretase density map (*Homo sapiens*, EMD-3061, protein complex, no symmetry and reported resolution of 3.4 Å) with a symmetry of C1 and several different resolution inputs (3.0 Å, 3.2 Å and 3.4 Å) and found the selected segments to be quite consistent. Running get_queries automatically with the resolution input of 3.2 Å yielded the best set of query models, and was used for query generation. Upon completion of get_queries, we inspected the resulting queries with the density maps in the Coot pop-up window and observed the queries were localized to two distinct regions with clean, continuous backbone density throughout, one region in the extracellular domains

(referred to as the extracellular region) and one region in the transmembrane domains (referred to as the transmembrane region). The first region contained three segments: two helices and one beta-strand, whose side-chain densities were easily distinguishable using the simplified six-letter code. get_queries successfully generated .pdb files with predicted query sequences for the three segments. We then manually inspected the query models, correcting residues incorrectly assigned by get_queries and extending the queries on both ends as the density permitted. This yielded the following degenerate sequences, which were then used for searching: (1) GGXGPLGGYLGWGXG; (2) LLYYGGGGPPGGXGGKGGXYGL; (3) GGGKGGXLGGGGGLXKGP.

Selecting and processing segments in the transmembrane region in the same way yielded query sequences for three helical segments: (1) GGKLGXGGGLGYXGGXGGYGG; (2) PYYLGGGYGGGXGLLYGYKGGGYXGGGGK; (3) LPXYGGGGLLGGYGGGGXLGXWGYG.

Using these two sets of query sequences, we tested the ability of cryoID to correctly identify the corresponding protein, first from a more limited candidate pool consisting of the 20,397 proteins in the *H. sapiens* proteome, and then against a much larger candidate pool consisting of the entire ~560,000 reviewed proteins in the UniProt database. When given the smaller 20,397 protein candidate pool, cryoID correctly identified the corresponding proteins for both of the query sets generated from the human gamma-secretase cryoEM map, correctly making a unique protein ID of Nicastrin (Q92542) for the extracellular-region query set and APH-1 (Q96BI3) for the transmembrane-region query set (Supplementary Tables 3 and 4). Against the much larger ~560,000 protein candidate pool, cryoID correctly identified APH-1 (Q96BI3) as the correct protein for the transmembrane-region query set (Supplementary Table 3), and Nicastrin as the correct protein for the extracellular-region query set (Supplementary Table 4).

cryoID and the NOMPC mechanotransduction channel. The NOMPC mechanotransduction channel from *D. melanogaster* is a homotetrameric integral membrane protein that mediates gentle-touch sensation. We tested get_queries on the NOMPC density map (*D. melanogaster*, EMD-8702, C4 symmetry, reported resolution 3.6 Å). The 3.2 Å and C4 symmetry input parameters yielded one region in the transmembrane domain with clean, continuous backbone density throughout, from which get_queries produced a set of three query sequences. We manually inspected the query models, correcting residues incorrectly assigned by get_queries and extending the queries on both ends as the density permitted. This yielded the following degenerate sequences, which were then used for searching: (1) WGGXLYLGGYGGYLLGGGGGGGLLGLKGGGYXKG; (2) LLXGGGKYLGGXGGYGLGYG; (3) GGXYGGXGGGYGYGLGXGGG.

Using this set of query sequences, we tested the ability of cryoID to correctly identify the corresponding protein, first from a more limited candidate pool consisting of the 3,500 proteins in the *D. melanogaster* proteome, and then against a much larger candidate pool consisting of the entire ~560,000 reviewed proteins in the UniProt database. In both cases, cryoID correctly identified the corresponding protein for the query set generated from the *Drosophila* NOMPC cryoEM map, correctly making a unique protein ID of NOMPC (E0A9E1) (Supplementary Table 2).

Benchmarking on new experimental structures obtained from *P. falciparum* parasites using the endogenous structural proteomics workflow.

We tested cryoID against two unpublished experimental cryoEM maps, which we obtained from *P. falciparum* parasite lysates using our endogenous structural proteomics workflow, yielding four maps at 3.2-Å, 3.2-Å, 3.48-Å and 3.67-Å overall resolutions. As a control for cryoID, we independently identified the proteins in the two 3.2-Å maps and built de novo atomic models into the two maps by hand. To identify the proteins in each map, we manually sorted through the 773 possible protein candidates identified by mass spectrometry, discarding all proteins that were too low in abundance, and all proteins that had the wrong symmetry, oligomeric state, size or overall structure based on published atomic models (including atomic models of known homologs from other organisms). After discarding all of the candidates that were obviously wrong, we were left with 5–10 potential candidates. We then compared published structures of the candidates or their homologs against our cryoEM maps until we found a structure for each that appear to fit well in the density.

In the case of our map that was ultimately determined to be M18 aspartyl aminopeptidase (Unknown Protein 1), the published crystal structure of M18 aspartyl aminopeptidase from *P. falciparum* (PDB accession code 4EME) fit perfectly into our density map. We further confirmed the protein ID by independently building into our Unknown Protein 1 cryoEM map de novo (that is, from scratch, building one residue at a time), using only the primary sequence of *P. falciparum* M18 aspartyl aminopeptidase as a guide. Our resulting atomic model matched the previously published crystal structure almost perfectly (RMSD = 0.55 Å).

In the case of our map that was ultimately determined to be glutamine synthetase (Unknown Protein 2), the published structure of a homolog, glutamine synthetase from *S. enterica*, fit well into our density map. In order to test whether our map was truly glutamine synthetase, we independently built into our Unknown Protein 2 cryoEM map de novo, using the primary sequence of *P. falciparum* glutamine synthetase as a guide. Our resulting atomic model

matched the *S. enterica* crystal structure well (RMSD = 1.5 Å), with the exception of a 50-residue long insertion near the active site.

In the meantime, we tested `get_queries` on the M18 aspartyl aminopeptidase density map, named Unknown Protein 1 (*P. falciparum*, Unknown Protein 1, T symmetry, reported resolution 3.2 Å), using a symmetry of T and a high resolution limit of 3.2 Å as the initial input parameters. We tuned the resolution parameter according to local resolution estimates and ultimately found 3.2 Å yielded the best results. We then manually inspected the query models, correcting residues incorrectly assigned by `get_queries` and extending the queries on both ends as the density permitted. This yielded the following degenerate sequences, which were then used for searching: (1) LGKGYLGGGLXYGKXKLGGLYLGGKXKLKLL; (2) GKYGLLGGGYGYGGYLLLL; (3) GGGXGYGGLLYLKKGKGGGGY.

Using this set of query sequences, we test the ability of `cryoID` to correctly identify the corresponding protein from a candidate pool consisting of the 773 proteins identified in this sucrose gradient fraction by mass spectrometry. `cryoID` correctly identified the corresponding protein for the query set generated from the Unknown Protein 1 cryoEM map, making a unique protein ID of M18 aspartyl aminopeptidase from *P. falciparum* (Q8I2J3) (Supplementary Table 6). We confirmed the identification by manually building a de novo atomic model into the rest of the map, and then comparing the resulting atomic model with the pre-existing published atomic model of the M18 aspartyl aminopeptidase from *P. falciparum*, solved by X-ray crystallography to 2.6 Å resolution (PDB accession code 4EME). Our de novo atomic model from our `cryoEM` map agreed well with the published model (RMSD 0.55 Å), serving as a gold standard validation of our workflow and `cryoID`'s performance.

We then tested `get_queries` on the glutamine synthetase density map, named Unknown Protein 2 (*P. falciparum*, Unknown Protein 2, D6 symmetry, reported resolution 3.2 Å), using a symmetry of D6 and a high resolution limit of 3.2 Å as the initial input parameters. We tuned the resolution parameter according to local resolution estimates⁵⁷ and ultimately found that 3.0 Å yielded the best results. We then manually inspected the query models, correcting residues incorrectly assigned by `get_queries` and extending the queries on both ends as the density permitted. This yielded the following degenerate sequences, which were then used for searching: (1) LGYGLLGGGYLYKYLKLL; (2) GGYKLPLGGGGXYLGGGLGLGGK; (3) PLGLGLYXLLGGKYLKGGGGGYGK; (4) YLGGPYLGGGLGGKLLKLGXL.

Using this set of query sequences, we tested the ability of `cryoID` to correctly identify the corresponding protein, from a candidate pool consisting of the 773 proteins identified in this sucrose gradient fraction by mass spectrometry. `cryoID` correctly identified the corresponding protein for the query set generated from the Unknown Protein 2 cryoEM map, making a unique protein ID of glutamine synthetase from *P. falciparum* (C0H551) (Supplementary Table 7). We confirmed the identification by manually building a de novo atomic model into the rest of the map, and then comparing the resulting atomic model with the pre-existing published atomic model of a close homolog, glutamine synthetase from *S. enterica*, solved by X-ray crystallography to 2.67-Å resolution (PDB accession code 1F1H). Our de novo atomic model from our `cryoEM` map agreed well with the *S. enterica* glutamine synthetase structure (RMSD 1.5 Å) throughout most of the structure, particularly in the active site. However, we do observe one major difference between the two structures (Fig. 5c–e).

Finally, we used `cryoID` to successfully identify the 3.48-Å and 3.67-Å maps to be the *P. falciparum* 20S proteasome from a candidate pool containing the entire *P. falciparum* proteome (Supplementary Tables 6 and 7). Furthermore, `cryoID` readily identified and distinguished between individual 20S proteasome subunits, enabling us to fit the previously published *P. falciparum* 20S proteasome model (PDB 5FMG)²⁴ into each of our two maps. Each residue in the model was then manually refit into each of our two maps in COOT to optimize geometry and fit. We were also able to build a number of previously unmodeled sections in many of the α and β subunits in both structures, thanks to improvements in local resolution or conformational differences in several regions throughout both maps. Comparison of our structures with the previously published *P. falciparum* 20S proteasome structure revealed several major differences, the most striking of which is the disordered $\beta 4$ and $\beta 5$ subunits in our 3.67-Å structure of the 20S proteasome- $\beta 4\beta 5_{flex}$ conformation.

Reporting Summary. Further information on research design is available in the Nature Research Reporting Summary linked to this article.

Data availability

The atomic models and the cryoEM density maps are deposited to the Protein Data Bank and the Electron Microscopy Data Bank, with the accession numbers 6PEV, 6PEW, EMD-20333 and EMD-20334. For raw image data, please contact the corresponding author. The proteomics data have been deposited to the ProteomeXchange Consortium (<http://proteomecentral.proteomexchange.org>) via the MassIVE partner repository with the dataset identifier PDX014263.

Code availability

`cryoID` is an open source program under the MIT license, available for download at github (<https://github.com/EICN-UCLA/cryoID>).

References

- Kaiser, P. & Wohlschlegel, J. Identification of ubiquitination sites and determination of ubiquitin-chain architectures by mass spectrometry. *Methods Enzymol.* **399**, 266–277 (2005).
- Kelstrup, C. D., Young, C., Lavalley, R., Nielsen, M. L. & Olsen, J. V. Optimized fast and sensitive acquisition methods for shotgun proteomics on a quadrupole orbitrap mass spectrometer. *J. Proteome Res.* **11**, 3487–3497 (2012).
- Tabb, D. L., McDonald, W. H. & Yates, J. R. 3rd DTASelect and contrast: tools for assembling and comparing protein identifications from shotgun proteomics. *J. Proteome Res.* **1**, 21–26 (2002).
- Xu, T. et al. ProLuCID: an improved sequest-like algorithm with enhanced sensitivity and specificity. *J. Proteom.* **129**, 16–24 (2015).
- Zheng, S. Q. et al. MotionCor2: anisotropic correction of beam-induced motion for improved cryo-electron microscopy. *Nat. Methods* **14**, 331–332 (2017).
- Rohou, A. & Grigorieff, N. CTFFIND4: Fast and accurate defocus estimation from electron micrographs. *J. Struct. Biol.* **192**, 216–221 (2015).
- Zhang, K. Gautomatch plugin (GitHub, 2016); <https://github.com/scipion-em/scipion-em-gautomatch>
- Pettersen, E. F. et al. UCSF chimera - a visualization system for exploratory research and analysis. *J. Comput. Chem.* **25**, 1605–1612 (2004).
- Emsley, P., Lohkamp, B., Scott, W. G. & Cowtan, K. Features and development of coot. *Acta Crystallogr. D.* **66**, 486–501 (2010).
- Coordinators, N. R. Database resources of the national center for biotechnology information. *Nucleic Acids Res.* **44**, D7–D19 (2016).
- Aurrecoechea, C. et al. PlasmoDB: a functional genomic database for malaria parasites. *Nucleic Acids Res.* **37**, D539–D543 (2009).
- Kelley, L. A., Mezulis, S., Yates, C. M., Wass, M. N. & Sternberg, M. J. E. The Phyre2 web portal for protein modeling, prediction and analysis. *Nat. Protoc.* **10**, 845–858 (2015).
- Chen, V. B. et al. MolProbity: all-atom structure validation for macromolecular crystallography. *Acta Crystallogr. D.* **66**, 12–21 (2010).
- Schrodinger, L. L. C. The PyMOL Molecular Graphics System, Version 1.8 (2015).
- Kucukelbir, A., Sigworth, F. J. & Tagare, H. D. Quantifying the local resolution of cryo-EM density maps. *Nat. Methods* **11**, 63–65 (2014).
- Rotkiewicz, P. & Skolnick, J. Fast procedure for reconstruction of full-atom protein models from reduced representations. *J. Comput. Chem.* **29**, 1460–1465 (2008).
- Swint-Kruse, L. & Brown, C. S. Resmap: automated representation of macromolecular interfaces as two-dimensional networks. *Bioinformatics* **21**, 3327–3328 (2005).

Acknowledgements

This research was supported in part by grants from National Institutes of Health (R01GM071940/AI094386/DE025567 to Z.H.Z. and K99/R00 HL133453 to J.R.B.). C.M.H. acknowledges funding from the Ruth L. Kirschstein National Research Service Award (AI007323). X.L. acknowledges funding from the China Scholarship Council (CSC). We thank the UCLA Proteome Research Center for assistance in mass spectrometry and acknowledge the use of resources in the Electron Imaging Center for Nanomachines supported by UCLA and grants from NIH (S10RR23057, S10OD018111 and U24GM116792) and NSF (DBI-1338135 and DMR-1548924).

Author contributions

C.M.H., A.W.P.F. and Z.H.Z. initiated the project; J.R.B. cultured and harvested parasite material; C.M.H. purified the sample from parasite pellets, screened purified samples by negative stain, optimized sample freezing conditions for cryoEM, acquired and processed the cryoEM data, interpreted the structures, designed the endogenous structural proteomics workflow, helped design `cryoID` and wrote the paper; M.L. built and refined the atomic models and helped interpret the structures; J.A.W. performed the mass spectrometry; C.M.H., X.L. and M.L. designed the `cryoID` workflow. X.L. developed and benchmarked `cryoID` and helped write the paper. X.L. and C.M.H. worked with T.C.T. to write and optimize the *Phenix* tool *sequence_from_map*. Z.H.Z. supervised the cryoEM aspects of the project, interpreted the structures and wrote the paper; D.E.G. supervised parasitology aspects of the project. A.W.P.F., M.L., T.C.T., J.R.B., J.A.W. and D.E.G. helped edit the paper; all authors approved the paper.

Competing interests

The authors declare no competing interests.

Additional information

Supplementary information is available for this paper at <https://doi.org/10.1038/s41592-019-0637-y>.

Correspondence and requests for materials should be addressed to Z.H.Z.

Peer review information Allison Doerr was the primary editor on this article and managed its editorial process and peer review in collaboration with the rest of the editorial team

Reprints and permissions information is available at www.nature.com/reprints.

Reporting Summary

Nature Research wishes to improve the reproducibility of the work that we publish. This form provides structure for consistency and transparency in reporting. For further information on Nature Research policies, see [Authors & Referees](#) and the [Editorial Policy Checklist](#).

Statistics

For all statistical analyses, confirm that the following items are present in the figure legend, table legend, main text, or Methods section.

n/a Confirmed

- ☐ ☒ The exact sample size (n) for each experimental group/condition, given as a discrete number and unit of measurement
- ☐ ☒ A statement on whether measurements were taken from distinct samples or whether the same sample was measured repeatedly
- ☐ ☒ The statistical test(s) used AND whether they are one- or two-sided
Only common tests should be described solely by name; describe more complex techniques in the Methods section.
- ☒ ☐ A description of all covariates tested
- ☒ ☐ A description of any assumptions or corrections, such as tests of normality and adjustment for multiple comparisons
- ☒ ☐ A full description of the statistical parameters including central tendency (e.g. means) or other basic estimates (e.g. regression coefficient) AND variation (e.g. standard deviation) or associated estimates of uncertainty (e.g. confidence intervals)
- ☒ ☐ For null hypothesis testing, the test statistic (e.g. F , t , r) with confidence intervals, effect sizes, degrees of freedom and P value noted
Give P values as exact values whenever suitable.
- ☒ ☐ For Bayesian analysis, information on the choice of priors and Markov chain Monte Carlo settings
- ☒ ☐ For hierarchical and complex designs, identification of the appropriate level for tests and full reporting of outcomes
- ☒ ☐ Estimates of effect sizes (e.g. Cohen's d , Pearson's r), indicating how they were calculated

Our web collection on [statistics for biologists](#) contains articles on many of the points above.

Software and code

Policy information about [availability of computer code](#)

Data collection

Leginon

Data analysis

MotionCor2, CTFFIND4, Gautomatch, CryoSPARC, RELION2.0, UCSF Chimera, Coot, PHENIX, Resmap, Molprobity, Pymol, Pulchra, IP2, cryoID

For manuscripts utilizing custom algorithms or software that are central to the research but not yet described in published literature, software must be made available to editors/reviewers. We strongly encourage code deposition in a community repository (e.g. GitHub). See the Nature Research [guidelines for submitting code & software](#) for further information.

Data

Policy information about [availability of data](#)

All manuscripts must include a [data availability statement](#). This statement should provide the following information, where applicable:

- Accession codes, unique identifiers, or web links for publicly available datasets
- A list of figures that have associated raw data
- A description of any restrictions on data availability

The atomic models and the cryoEM density maps have been deposited to the Protein Data Bank and the Electron Microscopy Data Bank, accession numbers 6PEV, 6PEW (PDB); EMD-20333, EMD-20334 (EMDB). The proteomics data have been deposited to the ProteomeXchange Consortium (<http://proteomecentral.proteomexchange.org>) via the MassIVE partner repository with the dataset identifier PDX014263.

Field-specific reporting

Please select the one below that is the best fit for your research. If you are not sure, read the appropriate sections before making your selection.

☒ Life sciences ☐ Behavioural & social sciences ☐ Ecological, evolutionary & environmental sciences

For a reference copy of the document with all sections, see [nature.com/documents/nr-reporting-summary-flat.pdf](https://www.nature.com/documents/nr-reporting-summary-flat.pdf)

Life sciences study design

All studies must disclose on these points even when the disclosure is negative.

Sample size	3D reconstructions were calculated from thousands of particle images. This number was determined based on resolutions measured by the Resmap program to be ~2.5-3.5 angstroms, with visible densities for different amino acid residue sidechains.
Data exclusions	About 70% of the total particle images were discarded after 2D and 3D classification using the program RELION. 328,435 particles were extracted from 2,514 micrographs. After several rounds of reference-free two-dimensional (2D) classification in RELION, poor quality particles that did not give rise to 2D class averages exhibiting clear secondary structure features were discarded.
Replication	All measurements were confirmed to be reproducible.
Randomization	Not applicable, our experiment does not involve allocation of samples/organisms/participants into experimental groups.
Blinding	Not applicable, our experiment does not involve group allocation.

Reporting for specific materials, systems and methods

We require information from authors about some types of materials, experimental systems and methods used in many studies. Here, indicate whether each material, system or method listed is relevant to your study. If you are not sure if a list item applies to your research, read the appropriate section before selecting a response.

Materials & experimental systems

n/a	Involved in the study
<input checked="" type="checkbox"/>	<input type="checkbox"/> Antibodies
<input type="checkbox"/>	<input checked="" type="checkbox"/> Eukaryotic cell lines
<input checked="" type="checkbox"/>	<input type="checkbox"/> Palaeontology
<input checked="" type="checkbox"/>	<input type="checkbox"/> Animals and other organisms
<input checked="" type="checkbox"/>	<input type="checkbox"/> Human research participants
<input checked="" type="checkbox"/>	<input type="checkbox"/> Clinical data

Methods

n/a	Involved in the study
<input checked="" type="checkbox"/>	<input type="checkbox"/> ChIP-seq
<input checked="" type="checkbox"/>	<input type="checkbox"/> Flow cytometry
<input checked="" type="checkbox"/>	<input type="checkbox"/> MRI-based neuroimaging

Eukaryotic cell lines

Policy information about [cell lines](#)

Cell line source(s)	The Plasmodium falciparum NF54attB line used in this study was obtained from the Fidock lab where it was generated.
Authentication	PCR amplified regions from the NF54attB genome were found to match the genome sequence for 3D7, a sub clone of NF54. The presence of the cg6 localized attB sequence was verified by successful Bxb1 integration at that site.
Mycoplasma contamination	Cell lines were not tested for mycoplasma contamination.
Commonly misidentified lines (See ICLAC register)	No commonly misidentified lines were used in the study.